ROYAL SOCIETY
OF CHEMISTRY

COMMUNICATION

Check for updates

A core−shell Cu₂O@Cu-MOF for electromagnetic wave absorption and selective shielding

Ji-You Zong,† Zhan-Zhan Wang,† Meng-Qi Wang, Jin-Cheng Shu,*
Wen-Qiang Cao [ID] * and Mao-Sheng Cao [ID] *

With the widespread adoption of emerging wireless technologies and devices, electromagnetic (EM) protection materials have become a global research focus. This study employs cuprous oxide (Cu_2O) cubes as templates and coats their surfaces with the conductive metal−organic framework (MOF)-copper hexahydroxytriphenylene (Cu-HHTP) to construct core−shell Cu_2O@Cu-HHTP. The material exhibits remarkable frequency-dependent EM characteristics, with both dielectric loss tangent and attenuation constant demonstrating peak values at 15.6 GHz that are considerably higher than those at other frequencies. Owing to these properties, Cu_2O@Cu-HHTP displays distinctive EM wave absorption and frequency-selective shielding capabilities. The material achieves a minimum reflection loss of −33.4 dB, with its effective EM wave absorption frequencies showing thickness-independent characteristics concentrated in the 13.6–17.0 GHz range. For EM shielding, it exhibits a shielding effectiveness difference of 19.8 dB and a transmission coefficient difference of 0.93. Furthermore, leveraging the superior EM attenuation of Cu_2O@Cu-HHTP, an EM energy conversion device is developed to harvest and reuse waste EM energy. This study not only expands the applications of conductive MOFs in EM protection, but also advances the development of high-performance EM protection materials with frequency-selective properties.

1. Introduction

The rapid advancement of 5G technology has facilitated the widespread application of electronic devices, while the emergence of artificial intelligence technology has further intensified this trend, leading to a continuous increase in electromagnetic (EM) wave radiation intensity in the environment. While offering convenience, such an EM environment may pose potential risks to human health, device operation,

School of Materials Science and Engineering, Beijing Institute of Technology, Beijing, 100081, China. E-mail: jc.shu@qq.com, wenqiang_cao@sina.com, caomaosheng@bit.edu.cn

† These authors are contributed equally to this work.

New concepts

This work introduces a core–shell Cu_2O@Cu-HHTP composite, where conductive metal–organic frameworks (MOFs) are integrated with inorganic templates for tailored electromagnetic (EM) protection. The breakthrough lies in its EM functionality—unique EM wave absorption and selective EM wave shielding—enabled by the distinctive frequency-dependent EM characteristics of Cu_2O@Cu-HHTP. Its effective EM wave absorption frequency is thickness-insensitive, overcoming the limitations of traditional absorbers. Its EM wave shielding exhibits strong frequency selectivity, with a transmittance difference of up to 0.93, avoiding the over-shielding issue of conventional shielding materials. This study reveals the advantages of conductive MOFs in developing EM protection materials, promoting the application of MOFs in EM functional materials and devices.

and information security.[1–7] In this context, EM protective materials with absorption or shielding capabilities have attracted considerable attention in recent years, making the development of high-performance EM protective materials an important research focus.[8–13]

Metal–organic frameworks (MOFs) are crystalline porous materials formed by coordination bonding between organic ligands and metal ions. Due to their unique bonding patterns, MOFs exhibit advantages such as a high surface area, tunable porosity, and customizable composition, making them widely applicable in gas separation and storage, catalysis, energy storage, and other fields, while also demonstrating significant potential in EM protection.[14–18] Despite these advantages, most pristine MOFs exhibit poor electrical conductivity, weak EM loss capability, and limited EM wave attenuation performance, making them unsuitable for direct use in EM protection. To address this issue, a common strategy involves subjecting MOFs to controlled thermal treatment to obtain conductive or magnetic MOF-derived materials.[19–21] For example, Liang *et al.* synthesized CoFe Prussian blue analogs (PBA) *via* a co-precipitation method, followed by pyrolysis under an argon atmosphere to obtain CoFe/C composites.[22] The CoFe-PBA exhibits negligible EM wave absorption performance. In contrast, the CoFe/C composite demonstrates enhanced dielectric

loss and magnetic loss capabilities, achieving a minimum reflection loss (RL) of −44.6 dB.

Although MOF derivatives demonstrate promising performance in EM protection applications, the pyrolysis process not only consumes substantial energy but may also lead to the loss of active organic functional groups and the collapse of their ordered internal structures, resulting in a notable reduction in porosity and specific surface area. Recent fundamental understanding of electron transfer mechanisms in MOFs has revealed that their electrical conductivity can be modulated through judicious design of organic linkers and metal nodes. This approach enhances polarization and conductive capabilities, leading to improved EM wave attenuation performance.[23–25] Takaishi *et al.* reported the first conductive MOF, designated as $Cu[Cu(pdt)_2]$ (pdt = 2,3-pyrazinedithiolate).[26] Conductive MOFs can retain the structural units, topological features, and chemical properties of conventional MOFs while achieving suitable electrical conductivity, demonstrating unique potential for EM protection applications. For instance, Shan *et al.* synthesized conductive MOFs, $M_3(HHTP)_2$ (M = Cu, Zn, Ni), *via* a hydrothermal method.[27] Among the three synthesized products, $Cu_3(HHTP)_2$ exhibited the highest electrical conductivity, achieving a minimum RL of −56.45 dB and an EAB of 5.76 GHz, nearly covering the entire Ku band. Additionally, structural engineering serves as a viable approach to optimize the EM protection performance of materials. Core–shell structured materials, owing to their distinctive multi-interface characteristics, contribute to enhanced polarization loss. The interfacial regions readily facilitate charge accumulation, generating interfacial polarization that converts EM energy into thermal energy, thereby improving EM wave absorption performance. For example, the core–shell Ni@C@ZnO material fabricated by Wang *et al.* possesses abundant interfaces and heterojunction layers, exhibiting a RL of −55.8 dB.[28]

Herein, core–shell cuprous oxide@copper hexahydroxytriphenylene ($Cu_2O@Cu$-HHTP) was fabricated by employing Cu_2O cubes as templates and coated with the conductive MOF-Cu-HHTP. The material demonstrates notable EM dispersion characteristics, exhibiting a peak dielectric loss tangent at 15.6 GHz that is significantly higher than that in other frequency ranges. These properties endow $Cu_2O@Cu$-HHTP with distinctive EM wave absorption performance and frequency-selective electromagnetic interference (EMI) shielding characteristics. The composite achieves a minimum RL of −33.4 dB, while maintaining thickness-insensitive absorption frequencies predominantly concentrated between 13.6 and 17 GHz. Regarding EMI shielding, the maximum shielding effectiveness difference reaches 19.8 dB, with a transmission coefficient difference of up to 0.93. Furthermore, a device capable of converting harmful EM energy into electrical energy was developed, presenting a novel approach to addressing EM pollution.

2. Results and discussion

The synthesis process of core–shell $Cu_2O@Cu$-HHTP is illustrated in Fig. 1(a). Under the reduction effect of ʟ-ascorbic

acid, regular-shaped Cu_2O nanocubes are obtained (Fig. 1(b)). As shown in Fig. 1(c) and (d), after treatment with the HHTP ligand, the product surface becomes covered with a layer of Cu-HHTP, and the edge length slightly increases. TEM analysis reveals that compared to Cu_2O (Fig. 1(e) and Fig. S1), the edge of $Cu_2O@Cu$-HHTP has a brighter area (Fig. 1(f)), while the inner layer is darker, confirming the presence of a Cu-HHTP coating on the Cu_2O surface. This is because under high-temperature reaction conditions, the Cu_2O nanocubes undergo partial dissolution, releasing copper ions that coordinate with HHTP to form a Cu-HHTP layer on the surface, ultimately yielding core–shell structured $Cu_2O@Cu$-HHTP. The surface Cu-HHTP layer is observed by HRTEM and fine microcrystals are found, as shown in Fig. 1(g).

EDS elemental mapping is employed to analyze the elemental distribution within the material. As shown in Fig. 1(h)–(l), both O and Cu elements originate from either Cu_2O or the surface HHTP ligand, while the C element exists exclusively in the HHTP ligand. This further confirms the successful coating of Cu-HHTP on the surface of the cubic Cu_2O. The Fourier-transform infrared (FTIR) spectra of different samples are shown in Fig. S2. The Cu_2O nanocubes exhibit absorption peaks only in the low wavenumber region, while the $Cu_2O@Cu$-HHTP nanocubes retain the absorption peaks of Cu_2O nanocubes and additionally show multiple peaks in the high wavenumber region. The FTIR results confirm the successful preparation of $Cu_2O@Cu$-HHTP and indicate the presence of abundant functional groups in $Cu_2O@Cu$-HHTP.

The crystal structure of $Cu_2O@Cu$-HHTP is analyzed by XRD measurements. As shown in Fig. 2(a), the material exhibits sharp diffraction peaks at $29.51°$, $36.39°$, $42.36°$ and $61.41°$, indicating the existence of a single crystal structure, which corresponds to the (110), (111), (200) and (220) crystal planes of Cu_2O (JCPDS no. 05-0667). Additionally, there are two relatively weak diffraction peaks at $9.47°$ and $12.61°$ (Fig. 2(b)), which are characteristic peaks of Cu-HHTP corresponding to its (200) and (210) crystal planes, further confirming the successful synthesis of Cu-HHTP.[29] Due to the thin layer of the MOF on the Cu_2O surface and its low crystallinity, the diffraction peaks of Cu-HHTP show relatively weak intensity.

The elemental valence states of Cu_2O and core–shell $Cu_2O@Cu$-HHTP are analyzed by XPS. As shown in Fig. S3 and S4, the Cu_2O nanocubes are composed of O and Cu, with copper existing in the Cu^+ valence state. As shown in Fig. 2(c), the XPS full spectrum reveals the presence of three elements: C, O, and Cu. As shown in Fig. 2(d), the C 1s spectrum exhibits peaks at 284.7 eV, 286.1 eV and 288.5 eV, corresponding to the C–C, C–O and C=O bonds, respectively. In Fig. 2(e), the peak at 530.6 eV is assigned to the O–Cu bond, while the peak at 531.8 eV corresponds to the O–C bond, and the peak at 536.6 eV is attributed to π–π interactions, confirming the existence of π conjugation.[30,31] Fig. 2(f) shows that copper ions exist in both Cu^+ and Cu^{2+} valence states. The two peaks at 932.5 eV and 934.6 eV correspond to the $2p_{3/2}$ states of Cu^+ and Cu^{2+}, respectively. The Cu^+ component originates partly from nano-Cu_2O and partly from the unsaturated Cu_1–O_2 centers in Cu-HHTP, while Cu^{2+} is exclusively derived from the saturated
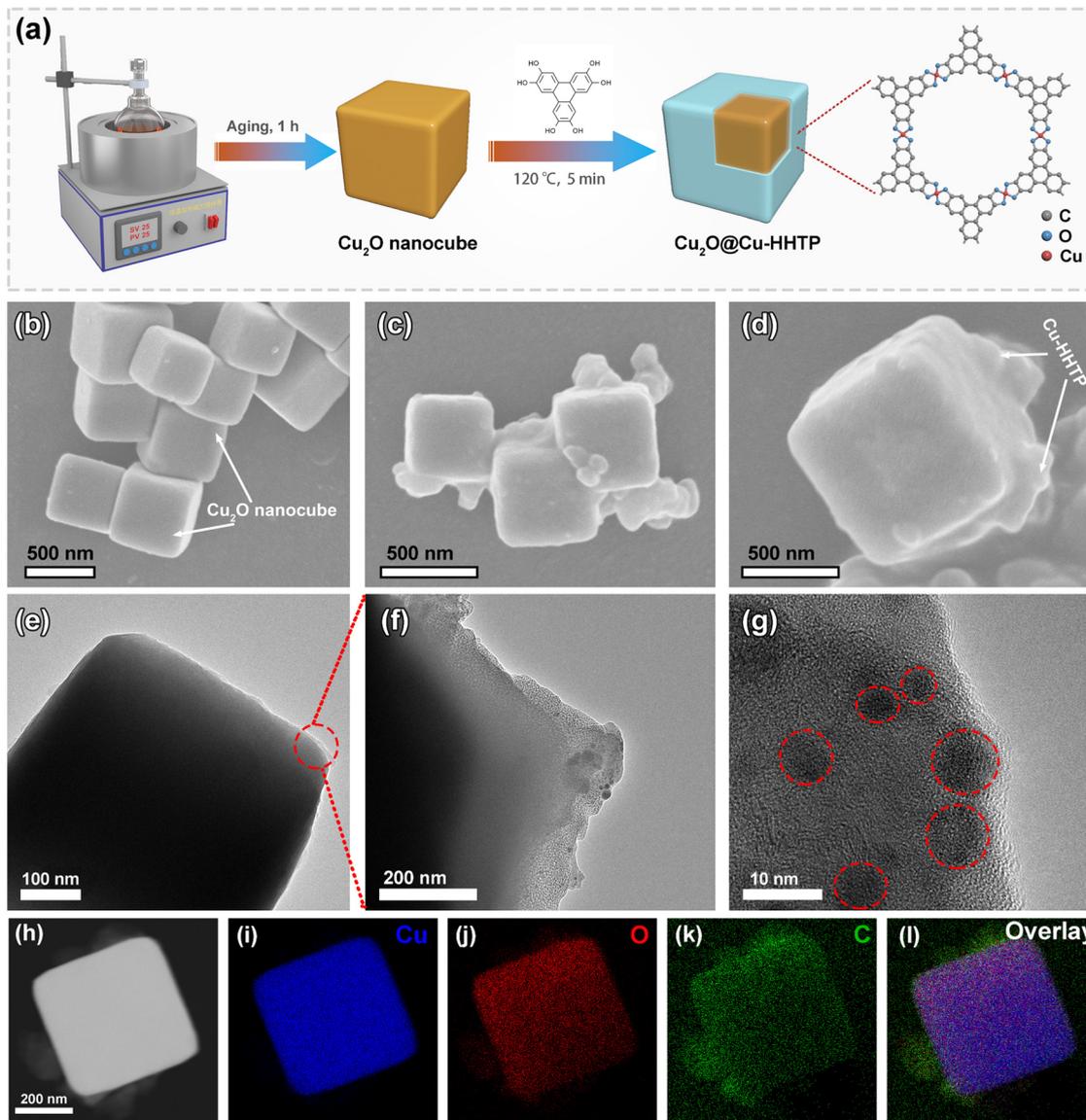
Fig. 1 (a) Schematic illustration of the synthesis process of Cu$_2$O@Cu-HHTP. SEM images of (b) Cu$_2$O and (c) and (d) Cu$_2$O@Cu-HHTP. TEM images of (e) Cu$_2$O and (f) and (g) Cu$_2$O@Cu-HHTP. (h)–(l) EDS elemental mapping of Cu$_2$O@Cu-HHTP.

Cu$_1$–O$_4$ centers in Cu-HHTP. Additionally, the peaks at 952.3 eV and 954.5 eV belong to the 2p$_{3/2}$ states of Cu$^+$ and Cu^{2+}, respectively, and the remaining peaks at 944.0 eV and 963.6 eV are satellite peaks.[32–34] The XPS results confirm the presence of conjugated bonds and abundant functional groups in the Cu-HHTP layer, which will lead to improvements in the dielectric properties of the material.

The EM protection performance of materials is closely related to their EM parameters. Cu$_2$O@Cu-HHTP is a non-magnetic material, and its EM protection performance depends mainly on its complex dielectric properties ($\varepsilon = \varepsilon' - j\varepsilon''$). Fig. 3(a) and (b) shows the complex permittivity of Cu$_2$O and Cu$_2$O@Cu-HHTP, which exhibit significant frequency dispersion characteristics. ε' displays a fluctuating trend in the 2–18 GHz range and increases with increasing filler concentration, with the 50 wt% sample showing the highest ε' value of 4.2. The imaginary part ε'' fluctuates around 0.2, showing multiple relaxation peaks, where the 50 wt% sample exhibits more obvious fluctuations with a maximum ε'' value of 2.3. The dielectric loss tangent ($\tan\delta$) and the attenuation constant (α) of samples at various concentrations show similar frequency dispersion characteristics. Among them, the 50 wt% sample demonstrates significantly higher $\tan\delta$ and α values at 15.6 GHz compared to those at other frequencies (Fig. 3(c) and (d)).

Furthermore, based on Debye theory, the dielectric loss ε'' of the 50 wt% sample is separated into two components: ε''_c contributed by conductivity and ε''_p contributed by relaxation.[35] Compared with conventional MOF materials, the enhanced conductivity of conductive MOFs originates from their unique structure. In Cu-HHTP, the coordination between Cu ions and hydroxyl groups of HHTP forms a two-dimensional honeycomb-like π-conjugated structure.[29] Strong interactions exist between
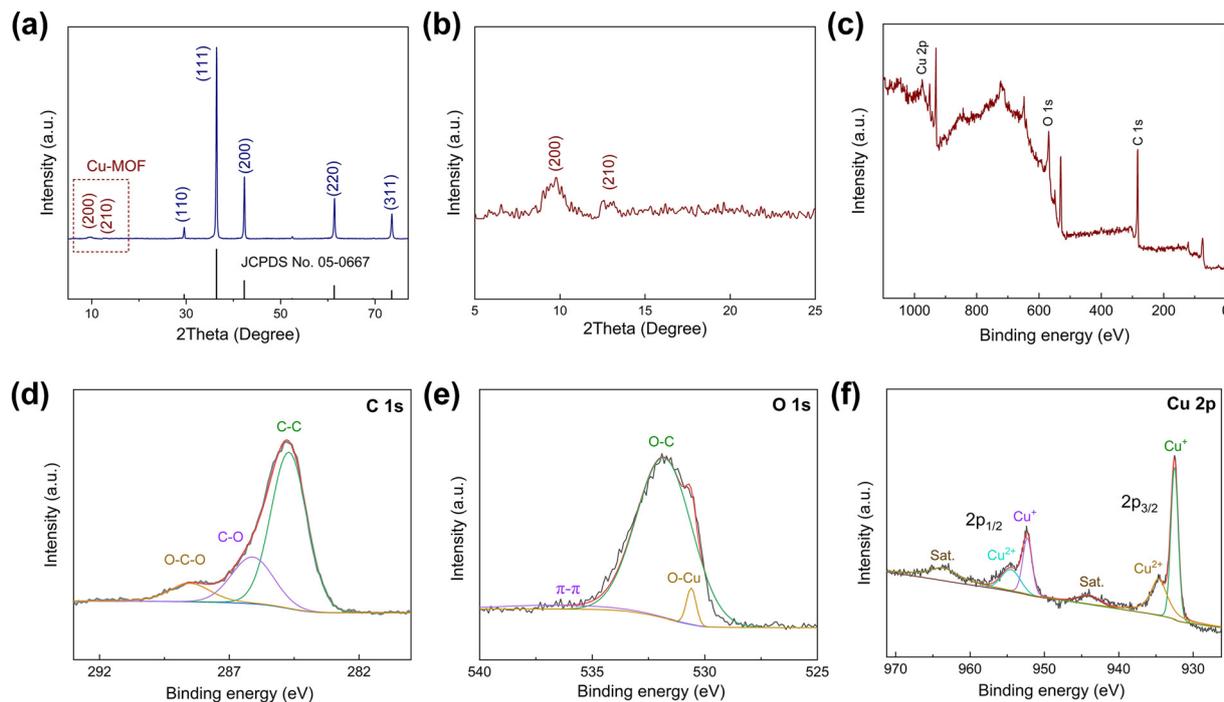
Fig. 2 (a) and (b) XRD pattern of Cu$_2$O@Cu-HHTP. (c) XPS full spectrum of Cu$_2$O@Cu-HHTP. (d) C 1s, (e) O 1s, and (f) Cu 2p spectra.

the d-orbitals of Cu ions and π-orbitals of HHTP, forming a d–π conjugated network. This conjugated network provides delocalization channels for electrons, enabling relatively free electron movement within the two-dimensional plane, thereby enhancing the conductivity of the materials.[36] Additionally, strong π–π stacking interactions exist between the two-dimensional conjugated layers. These stacking interactions cause a partial overlap of electron clouds between adjacent layers, providing pathways for interlayer electron transport.[37] In the core–shell Cu$_2$O@Cu-HHTP dispersion system, free charges transport through both migration and hopping mechanisms, during which EM energy is dissipated in the form of heat energy. The high conductivity facilitates improved conduction loss ε_c'' of the material toward EM waves. ε_c'' shows a strong frequency dependence, decreasing with increasing frequency (Fig. 3(e)).

The polarization loss ε_p'' curve of the material exhibits multiple relaxation peaks, with the peak intensities showing significant differences at different frequencies, demonstrating unique dispersion characteristics (Fig. 3(f)). To further investigate the polarization relaxation of the core–shell Cu$_2$O@Cu-HHTP, Cole–Cole curves are plotted based on the Debye theory, as shown in Fig. 3(g)–(i). Three semicircles are observed at 5.0 GHz, 10.1 GHz, and 15.2 GHz, confirming the existence of multiple relaxations. Within the coordination bonds of Cu-HHTP, there are two structures: saturated Cu$_1$–O$_4$ and unsaturated Cu$_1$–O$_2$.[29] Compared to Cu$_1$–O$_4$, the Cu$_1$–O$_2$ structure exhibits an asymmetric electron depletion region around the Cu atom, while adjacent O and C atoms show electron enrichment regions. Due to the presence of local polarization, relaxation polarization occurs when an external EM field is applied. In addition, the core–shell Cu$_2$O@Cu-HHTP creates a capacitor-

like structure between the Cu$_2$O core and Cu-HHTP shell interface, which also causes additional relaxation.[38]

The EM wave absorption performance of different samples at varying thicknesses within the 2–18 GHz range is calculated using the transmission line theory.[39] As shown in Fig. S5 and S6, the samples loaded with different Cu$_2$O contents exhibit poor electromagnetic wave absorption performance. As shown in Fig. 4(a)–(c), Cu$_2$O@Cu-HHTP with 30 wt% and 40 wt% loadings exhibits relatively low EM wave absorption performance and minimum RL values of only −9.9 dB and −10.7 dB, respectively. In contrast, the sample with 50 wt% loading demonstrates significantly enhanced absorption, achieving a minimum RL of −33.4 dB at a thickness of 2.9 mm. This improvement is primarily attributed to the higher dielectric polarization and loss capability of the 50 wt% sample, which results in stronger EM wave attenuation. Generally, the effective absorption frequency range of EM wave absorbing materials is closely related to the thickness, typically shifting toward lower frequencies as the thickness increases. Further analysis of the 50 wt% sample reveals that although its effective absorption range varies slightly with thickness, it is only distributed within 13.6–17 GHz, exhibiting an unusual insensitivity to thickness changes compared to conventional absorbers (Fig. 4(d) and Fig. S7).[5,39–43] The minimum RL values shift with thickness, and the corresponding frequencies consistently fall within the 13.6–17 GHz range (Fig. 4(e) and (f)). The EM wave absorption performance of the 50 wt% sample shows a strong frequency dependence and weak thickness sensitivity due to the unique dispersion characteristics of its composite dielectric constant, demonstrating the special potential of Cu$_2$O@Cu-HHTP in the field of EM wave absorption.
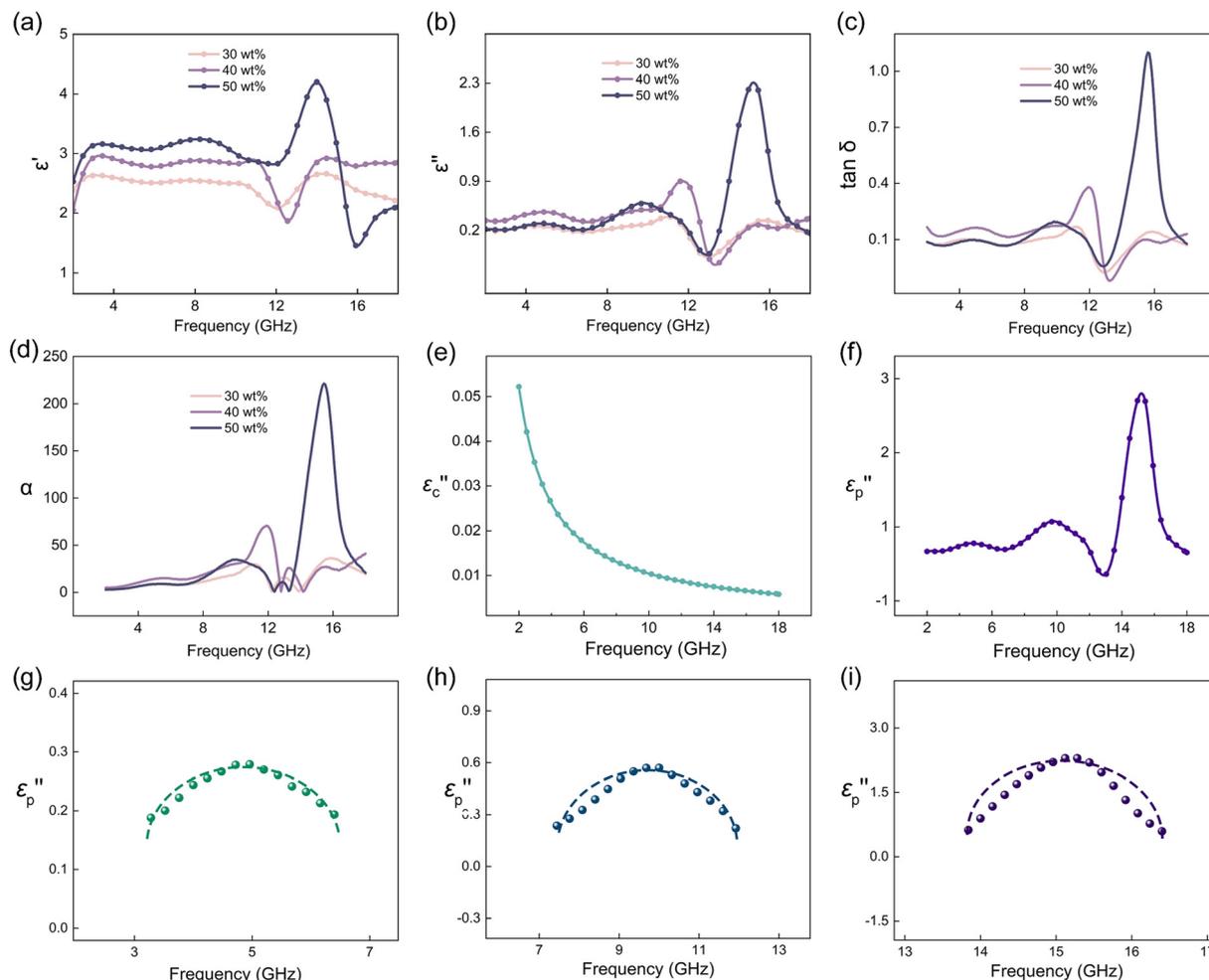
Fig. 3 (a) ε', (b) ε'', (c) tan δ, and (d) α curves of Cu$_2$O@Cu-HHTP with different loading contents of 30 wt%, 40 wt%, and 50 wt%. (e) ε''_c and (f) ε''_p curves of Cu$_2$O@Cu-HHTP with 50 wt%. (g)–(i) Cole–Cole plots.

Compared with traditional EMI shielding materials, selective EMI shielding materials can achieve efficient shielding in the target frequency band while avoiding signal blockage in non-target frequency bands, thereby addressing the issue of "over-shielding" associated with conventional broadband shielding materials. The EM properties of Cu$_2$O@Cu-HHTP exhibit notable frequency-dependent characteristics, which provide a foundation for developing selective EMI shielding materials. Fig. 5(a) shows the EMI shielding effectiveness (SE$_T$) of Cu$_2$O@Cu-HHTP in the 2–18 GHz range at different thicknesses. As the thickness increases, SE$_T$ improves significantly, reaching a maximum of 20.7 dB. SE$_T$ primarily consists of absorption effectiveness (SE$_A$) and reflection effectiveness (SE$_R$). As illustrated in Fig. 5(b) and (c), SE$_R$ remains lower than SE$_A$, with a maximum value of only 1.65 dB, indicating that the absorption capability of the Cu$_2$O@Cu-HHTP sample is significantly stronger than its reflection capability. The EMI shielding performance can be further analyzed based on the absorption coefficient (A), the reflection coefficient (R), and the transmission coefficient (T) (Fig. 5(d)–(f)). With increasing thickness, A generally increases, while T gradually decreases,

whereas R exhibits a more complex relationship with thickness. At certain frequencies, R reaches extreme values, which can be attributed to EM wave interference effects. However, under the same thickness and frequency conditions, R consistently remains lower than A, suggesting that absorption contributes more to shielding than reflection. The maximum A value reaches 0.9, while R remains as low as 0.06 (10 mm, 16 GHz). These results demonstrate that when external EM waves are incident, most of the energy is dissipated within the material rather than being reflected, thereby avoiding secondary EM pollution. Notably, the EMI shielding performance exhibits frequency selectivity, with the shielding effectiveness difference showing a strong thickness dependence. As shown in Fig. 5(g), analysis of the SE$_T$ at different thicknesses reveals that the peak shielding effectiveness consistently occurs around 15.5 GHz. Moreover, the shielding effectiveness in the target frequency band increases significantly with thickness, while remaining largely unaffected in non-target frequency bands. Fig. 5(h) summarizes the maximum, minimum, and average shielding values for samples of different thicknesses. The difference between maximum and minimum values is substantial,
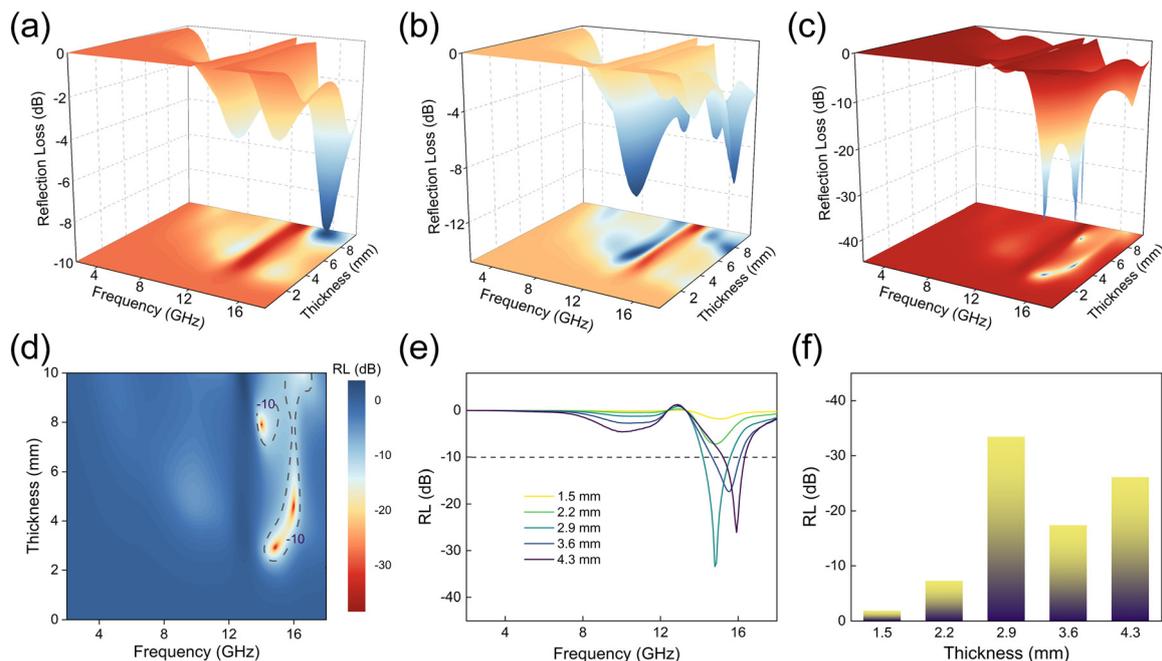
Fig. 4 (a)–(c) 3D plots of RL of Cu$_2$O@Cu-HHTP with different loading contents of 30 wt%, 40 wt%, and 50 wt%. (d) Projection diagram of RL of Cu$_2$O@Cu-HHTP with 50 wt%. (e) RL curves of Cu$_2$O@Cu-HHTP with 50 wt% at varying thicknesses. (f) Evaluation of minimum RL of Cu$_2$O@Cu-HHTP with 50 wt% at varying thicknesses.

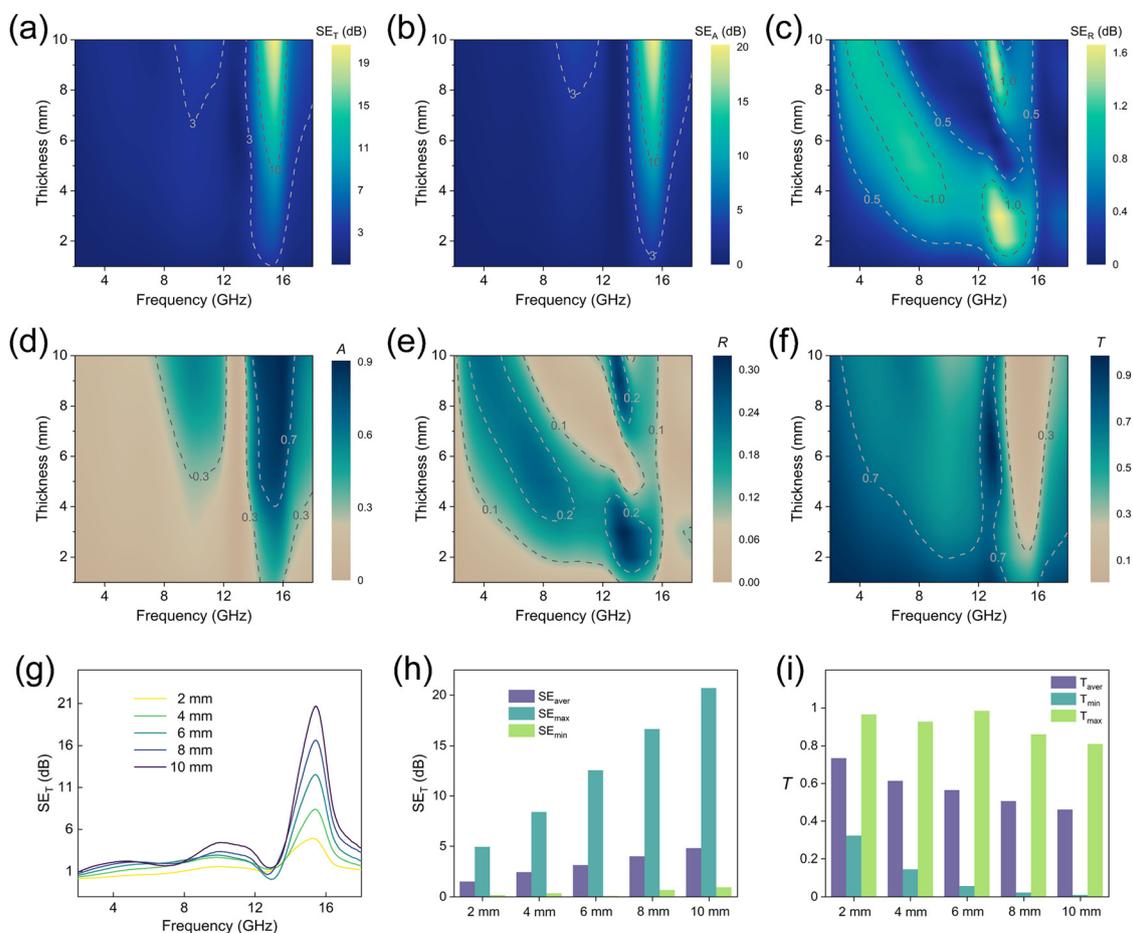**Fig. 5** EMI (a) SE$_T$, (b) SE$_A$, and (c) SE$_R$ curves of Cu$_2$O@Cu-HHTP with 50 wt%. (d) A, (e) R, and (f) T coefficients of Cu$_2$O@Cu-HHTP with 50 wt%. (g) EMI SE$_T$ curves of Cu$_2$O@Cu-HHTP with 50 wt% at different thicknesses. (h) Evaluation of maximum SE$_T$, minimum SE$_T$, and average SE$_T$ at different thicknesses. (i) Evaluation of maximum T, minimum T, and average T at different thicknesses.
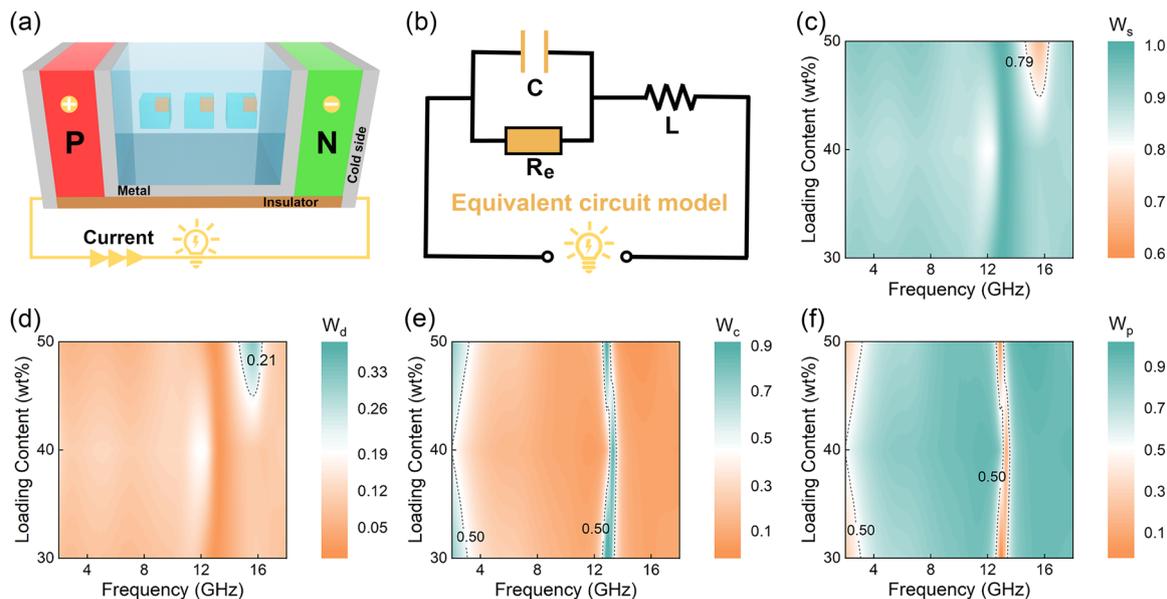
Fig. 6 (a) Schematic diagram of the EM energy conversion device. (b) Equivalent circuit model of the EM energy conversion device. (c) EM energy storage efficiency (W_s). (d) EM energy conversion efficiency. (e) Conduction loss contribution. (f) Relaxation loss contribution.

reaching up to 19.8 dB. Similarly, the transmission coefficient shows a maximum difference of 0.93 (Fig. 5(i)). As shown in Fig. S8, $Cu_2O@Cu$-HHTP demonstrates excellent frequency-selective EMI shielding performance compared to existing literature studies.[8,11,44,45]

Based on the outstanding EM attenuation characteristics of $Cu_2O@Cu$-HHTP, an EM energy conversion device is constructed, achieving the recovery and reuse of waste EM energy (Fig. 6(a)). The working principle of this device can be summarized as follows: when EM waves irradiate the absorption unit in the middle of the device, $Cu_2O@Cu$-HHTP converts EM energy into thermal energy through a dielectric loss mechanism. Subsequently, the generated thermal energy is transferred to adjacent metal plates, creating a temperature difference between the hot end and the cold end of the P–N semiconductor pair. According to the Seebeck effect, this temperature difference drives the generation of a thermoelectric current, thereby supplying power to external devices.[46,47] The physical mechanism can be elucidated in depth by establishing an equivalent circuit model (Fig. 6(b)): the absorption unit can be equivalently represented as a composite circuit composed of a resistor (R_e), a capacitor (C), and an inductor (L), where R_e dominates the EM energy conversion process, while C and L synergistically regulate the EM energy storage behavior.

An in-depth analysis of the EM energy conversion efficiency of the device is presented in Fig. 6(c)–(f). In the EM energy conversion device, the storage efficiency (W_s) and conversion efficiency (W_d) of EM energy are, respectively, defined as the ratios of stored and converted EM energy to absorbed EM energy, and they satisfy $W_s + W_d = 1$. As shown in Fig. 6(c) and (d), $W_s > W_d$, indicating that most of the EM energy is stored. Further mechanistic studies reveal that the converted EM energy can be divided into contributions from conduction loss (W_c) and relaxation loss (W_p). As illustrated in Fig. 6(e) and (f), the conduction loss caused by charge migration dominates the total dielectric loss behavior in the low-frequency range and at around 13 GHz. In summary, an EM energy conversion device based on the dielectric properties of $Cu_2O@Cu$-HHTP has been constructed, which is capable of converting waste EM energy into utilizable electrical energy, providing an innovative solution for the resource utilization of waste EM energy.

3. Conclusions

In summary, this study employed Cu_2O cubes as templates to fabricate core–shell $Cu_2O@Cu$-HHTP structures by coating their surfaces with a thin conductive MOF (Cu-HHTP) through coordination with HHTP ligands. The EM characteristics of $Cu_2O@Cu$-HHTP show notable frequency-dependent behavior, with both the dielectric loss tangent and the attenuation constant reaching peak values at 15.6 GHz that are significantly higher than those at other frequencies. Benefiting from these characteristics, $Cu_2O@Cu$-HHTP demonstrates distinctive EM wave absorption performance and frequency-selective shielding properties. The material achieves a minimum RL of −33.4 dB, while its effective absorption frequencies exhibit thickness-independent behavior, remaining concentrated within the 13.6–17 GHz range without significant variation with thickness. Regarding EMI shielding performance, the maximum shielding effectiveness difference reaches 19.8 dB, with a corresponding maximum transmission coefficient difference of 0.93. Owing to the favorable EM properties of $Cu_2O@Cu$-HHTP, a device capable of converting detrimental EM energy into electrical energy has been designed. This investigation contributes to

the advancement of EM protective materials, particularly frequency-selective EM protective materials.

4. Experimental section

4.1. Materials

Copper sulfate pentahydrate ($CuSO_4 \cdot 5H_2O$, 99.8%), sodium citrate trihydrate (99%), sodium hydroxide (NaOH, 95%), L-ascorbic acid (99%), N,N-dimethylformamide (99.5%), methanol (99.5%), and absolute ethanol (99%) were purchased from Shanghai Macklin Biochemical Technology Co., Ltd. Hexahydroxytriphenylene (97%) was obtained from Ron Reagent. Ultra-pure deionized water was used for all experiments.

4.2. Preparation of $Cu_2O@Cu$-HHTP

80 mL of deionized water was added to a round-bottomed flask and the flask was preheated in an oil bath at 25 °C. Subsequently, 375 mg of $CuSO_4 \cdot 5H_2O$ and 147 mg of sodium citrate trihydrate were sequentially added and stirred for 15 min to ensure complete dissolution. Then, 20 mL of NaOH solution (1.25 mol L^{-1}) was added and stirred continuously for 15 min. After that, 50 mL of L-ascorbic acid solution (0.03 mol L^{-1}) was added and the resulting solution was stirred continuously for 3 min. The reaction system was maintained at a constant temperature in the 25 °C oil bath and aged for 1 h. The product was alternately washed with deionized water and ethanol. Finally, it was separated by centrifugation and vacuum-dried at 60 °C for 12 h to obtain orange-red Cu_2O powder.

10 mg of the prepared Cu_2O powder was dispersed in a mixed solvent of 16 mL of N,N-dimethylformamide (DMF) and 600 μL of deionized water, followed by ultrasonication for 30 min to ensure its complete dispersion. Subsequently, 4 mL of DMF solution containing 8 mg of the hexahydroxytriphenylene (HHTP) ligand was added and stirred for 5 min until complete dissolution. The mixed solution was transferred to an oil bath stirrer preheated to 120 °C and stirred for 5 min. After the reaction, the product was washed with DMF and methanol, separated by centrifugation, and vacuum-dried at 60 °C for 12 h to obtain the core–shell structured $Cu_2O@Cu$-HHTP.

4.3. Material characterization

The morphology of the material was characterized by using scanning electron microscopy (SEM, Hitachi S-4800) and transmission electron microscopy (TEM, Tecnai G2 F30). The surface functional groups of the samples were determined by FTIR spectroscopy (Thermo-Smart-iTR). The crystal structure of the material was characterized by X-ray diffraction (XRD, Smart Lab, Cu Kα radiation). The valence states of elements were analyzed using X-ray photoelectron spectroscopy (XPS, PHI QUANTERA-II SXM).

4.4. Electromagnetic measurement

The sample was mixed with paraffin at 30 wt%, 40 wt%, and 50 wt% to form rings (inner diameter = 3.04 mm, outer diameter = 7.00 mm, and thickness = 2.00 mm). The EM parameters were tested within the range of 2–18 GHz using a vector network analyzer (VNA, ANRITSU 37269D).

Conflicts of interest

The authors declare no competing interests.

Data availability

All data generated or analyzed during this study are included in this published article and its SI.

Detailed testing and calculation processes of electromagnetic parameters and performance, TEM images, FTIR characterization results, XPS characterization results, and electromagnetic performance and comparison results. See DOI: https://doi.org/10.1039/d5nh00392j

Acknowledgements

References

1 J. L. Gao, L. Chang, B. Niu, X. C. Zhang, L. Li and M. S. Cao, *Adv. Compos. Hybrid Mater.*, 2024, **7**, 103.

2 W. D. Ma, Y. L. Li, P. Gong, Y. H. Jia and X. Fang, *Chin. Phys. B*, 2021, **30**, 107801.

3 X. Ma, F. Pan, Z. Xiu, L. Li, R. Zhang, H. Gu, C. Sun, Y. Gao and W. Lu, *Carbon*, 2024, **229**, 119444.

4 H. Xu, M. Liu, L. Huang, X. Zhang, Z. Ma, C. Zhu, F. Cao and Y. Chen, *Adv. Funct. Mater.*, 2025, 2502952.

5 J. L. Zhang, Z. Z. Wang, T. Y. Yang, S. Chatterjee, M. S. Cao and H. S. Peng, *Carbon*, 2024, **226**, 119199.

6 W. Wang, B. Ibarlucea, C. Huang, R. Dong, M. Al Aiti, S. Huang and G. Cuniberti, *Nanoscale Horiz.*, 2024, **9**, 1432–1474.

7 J. Y. Zong, H. Z. Zhai, H. Z. Guan, Z. Z. Wang, M. S. Cao and W. Q. Cao, *Adv. Funct. Mater.*, 2025, e07277.

8 X. X. Wang, H. T. Wu, W. S. Wang, Y. Luo and Y. J. Zheng, *Carbon*, 2023, **213**, 118267.

9 Y. Shen, Z. Ma, F. Yan, C. Zhu, X. Zhang and Y. Chen, *Adv. Funct. Mater.*, 2025, **35**, 2423947.

10 Y. Zhu, T. Liu, L. Li and M. Cao, *Nano Res.*, 2023, **17**, 1655–1665.

11 W. Cao, Z. Wang, X. Wan, T. Liu, C. Cao and M. Cao, *Adv. Compos. Hybrid Mater.*, 2024, **7**, 187.

12 J. C. Shu, W. Q. Cao and M. S. Cao, *Adv. Funct. Mater.*, 2021, **31**, 2100470.

13 S. Rostami, A. Ghaffarkhah, S. A. Hashemi, S. Wuttke, O. J. Rojas and M. Arjmand, *Nanoscale Horiz.*, 2024, **9**, 2234–2247.

14 J. Chen, P. Chen, B. Lei, Y. Hou, Z. Li, J. Lei and D. Zhao, *Carbon*, 2024, **230**, 119628.

15 M. Q. Wang, J. C. Shu, X. Wan, W. Q. Cao and M. S. Cao, *Small*, 2023, **19**, e2303186.

16 M. Q. Wang and M. S. Cao, *J. Mater. Sci. Technol.*, 2025, **214**, 37–52.

17 J. Zhu, Y. Cen, H. Ma, W. Lian, J. Liu, H. Ou, F. Ouyang, L. Zhang and W. Zhang, *Nanoscale Horiz.*, 2023, **8**, 1273–1281.

18 C. Guan, X. Liu, A. M. Elshahawy, H. Zhang, H. Wu, S. J. Pennycook and J. Wang, *Nanoscale Horiz.*, 2017, **2**, 342–348.

19 Y. Guo, Y. Duan, X. Liu, J. Tian, N. Wen, Z. Fan and L. Pan, *Carbon*, 2024, **230**, 119591.

20 Z. Z. Wang, Q. Zheng, M. J. Yu and M. S. Cao, *J. Mater. Sci. Technol.*, 2025, **228**, 1–10.

21 X. X. Fan, Z. Z. Wang, X. C. Zhang, L. Li and M. S. Cao, *Mater. Chem. Front.*, 2025, **9**, 403–417.

22 X. H. Liang, G. H. Wang, W. H. Gu and G. B. Ji, *Carbon*, 2021, **177**, 97–106.

23 X. Zhang, X. L. Tian, Y. T. Qin, J. Qiao, F. Pan, N. Wu, C. X. Wang, S. Y. Zhao, W. Liu, J. Cui, Z. Qian, M. T. Zhao, J. R. Liu and Z. H. Zeng, *ACS Nano*, 2023, **17**, 12510–12518.

24 X. Zhang, X. Tian, N. Wu, S. Zhao, Y. Qin, F. Pan, S. Yue, X. Ma, J. Qiao, W. Xu, W. Liu, J. Liu, M. Zhao, K. K. Ostrikov and Z. Zeng, *Sci. Adv.*, 2024, **10**, eadl6498.

25 H. Jin, M. Liu, L. Wang, W. You, K. Pei, H.-W. Cheng and R. Che, *Natl. Sci. Rev.*, 2025, **12**, nwae420.

26 M. Sasaki, H. Wu, D. Kawakami, S. Takaishi, T. Kajiwara, H. Miyasaka, B. K. Breedlove, M. Yamashita, H. Kishida, H. Matsuzaki, H. Okamoto, H. Tanaka and S. Kuroda, *Inorg. Chem.*, 2009, **48**, 7446–7451.

27 Z. Shan, S. Y. Cheng, F. Wu, X. H. Pan, W. J. Li, W. Dong, A. M. Xie and G. Zhang, *Chem. Eng. J.*, 2022, **446**, 137409.

28 L. Wang, X. F. Yu, X. Li, J. Zhang, M. Wang and R. C. Che, *Chem. Eng. J.*, 2020, **383**, 123099.

29 W. Cheng, H. Zhang, D. Luan and X. W. D. Lou, *Sci. Adv.*, 2021, **7**, eabg2580.

30 L. Sun, M. G. Campbell and M. Dincă, *Angew. Chem., Int. Ed.*, 2016, **55**, 3566–3579.

31 Y. Nakayama, T. Takahagi, F. Soeda, A. Ishitani, N. Kosugi and H. Kuroda, *J. Polym. Sci., Part A: Polym. Chem.*, 2003, **28**, 1813–1821.

32 K. W. Nam, S. S. Park, R. dos Reis, V. P. Dravid, H. Kim, C. A. Mirkin and J. F. Stoddart, *Nat. Commun.*, 2019, **10**, 4948.

33 J. Ghijsen, L. H. Tjeng, J. van Elp, H. Eskes, J. Westerink, G. A. Sawatzky and M. T. Czyzyk, *Phys. Rev. B: Condens. Matter Mater. Phys.*, 1988, **38**, 11322–11330.

34 T. Zhang, X. Nie, W. Yu, X. Guo, C. Song, R. Si, Y. Liu and Z. Zhao, *iScience*, 2019, **22**, 97–108.

35 H. Z. Guan, J. Y. Zong, M. Q. Wang, H. Z. Zhai, J. Yuan and M. S. Cao, *Carbon*, 2024, **226**, 119239.

36 L. Niu, T. Wu, M. Chen, L. Yang, J. Yang, Z. Wang, A. A. Kornyshev, H. Jiang, S. Bi and G. Feng, *Adv. Mater.*, 2022, **34**, 2200999.

37 G. Xu, C. Zhu and G. Gao, *Small*, 2022, **18**, 2203140.

38 M. S. Cao, J. Yang, W. L. Song, D. Q. Zhang, B. Wen, H. B. Jin, Z. L. Hou and J. Yuan, *ACS Appl. Mater. Interfaces*, 2012, **4**, 6949–6956.

39 X. Liu, S. Wang, J. Qiu, Q. Wang, R. Wang and W. Wang, *Carbon*, 2024, **230**, 119696.

40 F. Wu, F. Hu, P. Hu, P. Zhang, B. Fan, H. Kong, W. Zheng, L. Cai and Z. Sun, *Carbon*, 2024, **230**, 119644.

41 M. He, X. Zhong, X. Lu, J. Hu, K. Ruan, H. Guo, Y. Zhang, Y. Guo and J. Gu, *Adv. Mater.*, 2024, **36**, 2410186.

42 S. Chen, C. Cui, J. Yan, C. Lin, S. Jiang, H. Tang and R. Guo, *Carbon*, 2024, **230**, 119617.

43 X. Y. Ren, Y. H. Song, Z. G. Gao, Y. L. Wu, Z. R. Jia and G. L. Wu, *J. Mater. Sci. Technol.*, 2023, **134**, 254–261.

44 Y. Wu, Q. Li, Y. Li, C. Li, Y. Zhou, P. Du, W. Cao, X. He, Z. Liu, J. Xu, K. Huang, M. Lei, K. Bi and H. Wu, *Carbon*, 2024, **229**, 119474.

45 J. Qiu, C. Peng, R. Wang, C. Yao, X. Liu, Q. Wang and W. Wang, *Carbon*, 2024, **217**, 118610.

46 T. Liu, Q. Zheng, W. Cao, Y. Wang, M. Zhang, Q. Zhao and M. Cao, *Adv. Compos. Hybrid Mater.*, 2024, **7**, 79.

47 Q. Zheng, J. Q. Wang, W. Q. Cao, H. Z. Zhai and M. S. Cao, *Adv. Funct. Mater.*, 2025, **35**, 2417972.